Estimation Error Bound of Battery Electrode Parameters With Limited Data Window

Suhak Lee, Peyman Mohtat, Jason B. Siegel, *Member, IEEE*, Anna G. Stefanopoulou, *Fellow, IEEE*, Jang-Woo Lee, and Tae-Kyung Lee

***Abstract*—Advanced battery management system, which leverages an in-depth understanding of the battery state of health, can improve efficiently and safely. To this end, we introduce the electrode-level battery state of health (eSOH) estimation problem with open-circuit voltage (OCV) data. In real-world applications, collecting the full-range OCV data is difficult since the battery is not deeply discharged. When data is limited, the estimation accuracy deteriorates. In this article, we quantify the uncertainty of the electrode parameter estimation with partial data based on the Cramer–Rao bound and confidence interval. By introducing a voltage constraint in the estimation problem, the positive electrode parameters can be estimated with sufficient accuracy over a wide range of state of charge. However, the estimation accuracy of the negative electrode parameters is more sensitive to the depth of discharge. The proposed framework can be used as a guideline for selecting proper data windows and understanding the impact on parameter estimation.**

***Index Terms*—Estimation error bound, battery electrode parameters, Cramer-Rao bound, confidence interval, data window.**

I. Introduction

ELECTRIC vehicles (EV) and energy storage systems (ESS) require durability and reliability of their battery over their long service life. This requirement has motivated extensive research efforts on the estimation techniques for the state of health (SOH) of lithium-ion (Li-ion) batteries. Conventional SOH estimations seek to identify capacity fade or resistance increase of a cell as a lumped parameter. However, they fail to provide detailed information on the degradation status of a cell. Hence, electrode-specific SOH estimation is crucial for conducting advanced diagnosis with battery management system (BMS).

There have been many attempts by the modeling and simulation community to explain the observed cell-level degradation effects by assuming a specific aging mechanism in the detailed electrochemical model, such as loss of lithium due to the growth of solid electrolyte interphase (SEI) layer [1]. Developing diagnostic tools based on the physics-based model is challenging due to the complexity of the models [2]. To address this challenge, several studies have explored simple but accurate models at the open-circuit voltage (OCV) condition. Since the OCV is simply the voltage difference between the half-cell potential of positive and negative electrodes (PEs and NEs), it provides a thermodynamic fingerprint of each electrode without complex electrochemical dynamics such as diffusion and lithium intercalation. Thus, the degradation of the electrode can be identified by matching the changes of the aged OCV curve to the individual electrode potentials.

In literature, the approach of applying least-square fitting with the simple OCV model and pseudo-OCV data for the electrode parameter estimation has been experimentally validated in many studies [3]–[7]. Dubarry *et al.* [3] explained the electrode contributions to the cell OCV curve for various degradation modes by simulating a mechanistic model with electrode half-cell potentials. Birkl *et al.* [4] showed excellent diagnostic results with multiple coin-cells representing different levels of degradation modes, namely, loss of active material (LAM) and loss of lithium inventory (LLI). Similarly, Han *et al.* [5] and Lee *et al.* [6] characterized the cell OCV model with specific electrode SOH (eSOH) parameters, electrode capacity and utilization range. Dey *et al.* [7] modeled the dynamics of individual electrodes with the open-circuit potential (OCP) of both electrodes and internal resistance and proposed a real-time estimation scheme for electrode-level health estimation.

The remaining challenge is the OCV measurement. Despite a few ongoing efforts [8], taking exact OCV measurements is, in general, time-consuming and often not practical in many applications. Instead, it has been reported that a slow rate (e.g., C/20: a current rate of 20 h from a fully charged to a fully discharged state) of constant current–voltage measurement can be considered as pseudo-OCV. A survey [9] shows that battery-powered plug-in electric vehicles equipped with larger than 28 kWh battery pack would take at least 20 h to charge the battery fully from empty with 1.4 kW of level 1 charger, which is sufficiently slow to be used for this type of approach. Thus, one possible option for electrified vehicles is that the BMS requests a slow-charging protocol occasionally, when the driver allows it, to enable the eSOH parameter estimation. Another possibility is to record the rest voltage at key-ON so that the terminal voltage measurement can be considered as the OCV. Then, the collection of the OCV points at different state of charge (SOC) can be used for the estimation.

Manuscript received September 30, 2019; accepted October 20, 2019. Date of publication November 18, 2019; date of current version February 6, 2020. This work was supported by Samsung SDI Company, Ltd. Paper no. TII-19-4479. *(Corresponding author: Suhak Lee.)*

S. Lee, P. Mohtat, J. B. Siegel, and A. G. Stefanopoulou are with the Department of Mechanical Engineering, University of Michigan, Ann Arbor, MI 48109 USA (e-mail: suhaklee@umich.edu; pmohtat@umich.edu; siegeljb@umich.edu; annastef@umich.edu).

J.-W. Lee and T.-K. Lee are with the System Development Team, Samsung SDI Company, Ltd., Yongin-si 17084, South Korea (e-mail: jw.jay.lee@samsung.com; logos.lee@samsung.com).

Color versions of one or more of the figures in this article are available online at http://ieeexplore.ieee.org.

Digital Object Identifier 10.1109/TII.2019.2952066

The limitation from the OCV measurement becomes a motivation for this article in light of partial data availability. When such data are limited, the estimation suffers from the loss of accuracy; hence, the reliability of the estimation results has to be questioned. Most of the previous studies were conducted on a full range of OCV data for the eSOH estimation. Moreover, since the OCV curve is nonlinear, the estimation uncertainty must be analyzed for different span and region of depth of discharge (DOD). In literature, prior work used the Fisher information matrix-based Cramer–Rao bound (CRB) to evaluate the parameters' identifiability. Cell-level lumped parameters, such as cell capacity and internal resistance, are investigated using an equivalent circuit model [10]–[13]. Extending toward electrochemical model parameter estimation, Edouard *et al.* [14] presented a sensitivity analysis of its physical parameters to find out their influence on the output voltage. Similarly, Forman *et al.* [15] proposed a multiobjective genetic algorithm associated with the Fisher identifiability analysis for parameter identification. However, the estimation uncertainty of the eSOH-related parameters has not yet been studied. The scope of this article is to provide a quantitative metric for the estimation uncertainty of the eSOH parameters, when the OCV data is partially available.

II. Parameterization of Open-Circuit Voltage

This section describes the relationship of the OCV model and the electrode parameters that are related to individual eSOH. This relationship is used for the error bound derivation in Section III. When a cell is at equilibrium state, the terminal voltage of a cell is equal to the OCV, which is the difference between the OCP of positive and NEs. The OCP of each electrode is a function of the stoichiometric state y and x for the positive and NEs, respectively. For a Li-ion battery with lithium metal oxide $LiMO_2$ for the PE and graphite C_6 for the NE, as the cell is charging (c in backward reaction), the stoichiometric state x in the graphite increases. This increase is balanced with decreases in the stoichiometric state y in the metal oxide. Likewise, as the cell is discharging, the forward reaction occurs at each electrode as follows:

$$\mathrm{Li_xC_6} \underset{c}{\overset{d}{\rightleftharpoons}} \mathrm{xLi^+} + \mathrm{xe^-} + \mathrm{C_6}$$

$$\mathrm{Li_yMO_2} + (1-\mathrm{y})\mathrm{Li^+} + (1-\mathrm{y})\mathrm{e^-} \underset{c}{\overset{d}{\rightleftharpoons}} \mathrm{LiMO_2}.$$

The stoichiometric states x and y represent the fraction of filled sites in each electrode material. For example, a fully lithiated graphite is $x = 1$ for $\mathrm{Li_xC_6}$, i.e., one lithium atom per six carbon atoms. Then, the OCV is the electrical potential difference between the OCP of PE $U_p(y)$ and NE $U_n(x)$

$$V_{oc}(z) = U_p(y) - U_n(x) \tag{1}$$

where z is the DOD of the cell (i.e., DOD $= 1-$SOC) and satisfies the following relationship with the stoichiometric state of each electrode x and y where their range $x \in [x_0, x_{100}] \subset [0, 1]$ and $y \in [y_0, y_{100}] \subset [0, 1]$,

$$z = \frac{Q}{C} = \frac{y - y_{100}}{y_0 - y_{100}} = \frac{x_{100} - x}{x_{100} - x_0} \tag{2}$$

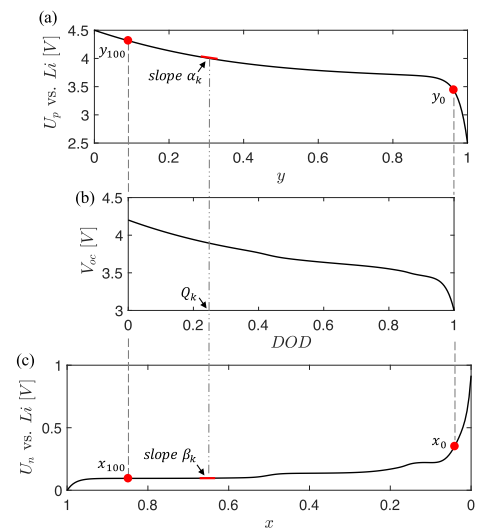

Fig. 1. Half-cell potential of individual electrodes and OCV of a cell with indication of the utilization range $[y_{100}, y_0]$, $[x_{100}, x_0]$. (a) Half-cell potential of nickel–manganese–cobalt (NMC) oxide for the positive electrode. (b) Cell OCV with respect to depth of discharge (DOD). (c) Half-cell potential of graphite for the negative electrode. Local slopes of half-cell potential α_k, β_k are depicted associated with the cell DOD Q_k.

where Q is the discharge Amp-hours from fully charged state obtained by coulomb counting and C is the cell capacity defined by upper $V_{\max}$ and lower $V_{\min}$ voltage limits satisfying

$$V_{\max} = U_p(y_{100}) - U_n(x_{100}) \tag{3}$$

$$V_{\min} = U_p(y_0) - U_n(x_0) \tag{4}$$

where subscripts 100 and 0 indicate the stoichiometric states at both ends of utilization range at upper and lower voltage limits, respectively. The battery manufacturer specifies the voltage limits to prevent the overcharge or over-discharge, and thus the individual electrodes are not fully utilized. Note that the upper voltage limit $V_{\max}$ is often expected in practice through typical constant current constant voltage (CCCV) charging protocol rather than the lower voltage limit $V_{\min}$. Then, the following equality holds for the capacities of individual electrodes, C_p for PE and C_n for NE, with respect to the cell capacity C

$$C = C_p(y_0 - y_{100}) = C_n(x_{100} - x_0). \tag{5}$$

Combining (2) and (5), the stoichiometric state of each electrode can be written as a function of Q

$$y = y_{100} + \frac{Q}{C_p}, \quad x = x_{100} - \frac{Q}{C_n}. \tag{6}$$

Finally, (1) can be written as a function of the discharge Amp-hours Q with the electrode parameters (i.e., electrode capacity and utilization range) $\theta = [y_{100}, C_p, x_{100}, C_n]$,

$$V_{oc}(Q;\theta) = U_p\left(y_{100} + \frac{Q}{C_p}\right) - U_n\left(x_{100} - \frac{Q}{C_n}\right). \tag{7}$$

Graphical interpretation of the OCV model is shown in Fig. 1. The upper utilization ranges of both electrodes y_{100} and x_{100} are aligned with the fully charged state of the cell. The capacities of the individual electrodes scale the electrode OCP with respect to the cell capacity axis.

III. Methodology: Derivation of Error Bound

In this section, the mathematical derivation of the analytic error bound is presented. First, the method for the electrode parameter estimation associated with equations for degradation diagnosis is introduced. After that, the error bounds are derived by the CRB and confidence interval.

A. Parameter Estimation and Degradation Diagnosis

The estimation is formulated as a nonlinear least-squares problem shown in (8a) since the OCV model in (7) is a nonlinear static equation. Other approaches such as peak matching [6] may produce different error bounds. The cell operates between the predefined voltage limits, and thus $V_{\max}$ is used as an equality constraint in (8b), which provides additional information to find the unknown parameters. The impact of the equality constraint on the estimation accuracy will be discussed.

$$\underset{\theta}{\text{minimize}} \quad \sum_{i=1}^{n} \left\| V_{oc}(Q_i;\theta) - V_{oc,i}^{data} \right\|^2 \tag{8a}$$

$$\text{subject to} \quad V_{\max} = U_p(y_{100}) - U_n(x_{100}). \tag{8b}$$

Due to the nonlinearity of the OCV model, the estimation problem becomes a nonconvex optimization problem with respect to the electrode parameters, and thus local minima could exist. To find an optimum solution, multiple initial guesses are generated within feasible bounds for the electrode parameters and provided to optimization solver. A parameter set providing the smallest cost function value is determined as an estimate. For instance, out of 100 randomly generated start points, we have observed that 55 start points converged to the same solution providing the minimum function value. The feasible bounds were given for the electrode parameters $\theta = [y_{100}, C_p, x_{100}, C_n]$ that are $x, y \in [0, 1]$ and $C_p, C_n \in [C, 2C]$ (electrode capacity is typically larger than cell capacity).

This approach requires accurate knowledge of the half-cell OCPs of both electrodes. In general, these half-cell potentials can be directly measured from coin-cell terminal voltage or found from the literature. The coin-cell takes one of the electrodes as a cathode and a thin lithium metal as a reference electrode. In case the half-cell potentials are not accurate (e.g., cell-to-cell variance, aging), the model will cause additional error in the parameter estimation. Our preliminary work shows that, in an NMC chemistry, the PE upper utilization y_{100} has the highest sensitivity to model mismatch. However, the propagation of the model mismatch to the parameter estimation is not in the scope of this article and it will be investigated in future work.

Furthermore, it is worth mentioning that the cell capacity C can be also estimated by incorporating the lower voltage limit $V_{\min}$ constraint. Once the electrode parameters are identified, it is possible to find a specific Amp-hours $Q = C$ that satisfies the lower voltage limit as shown below:

$$V_{\min} = U_p\left(\hat{y}_{100} + \frac{C}{\hat{C}_p}\right) - U_n\left(\hat{x}_{100} - \frac{C}{\hat{C}_n}\right). \tag{9}$$

Identification of electrode SOH and corresponding degradation modes is done by tracking the changes of the electrode parameters $\theta = [y_{100}, C_p, x_{100}, C_n]$ as a cell ages [16]. For aging diagnosis, we refer to commonly defined degradation modes: LLI in a cell and LAM for each electrode [3], [4]. LLI represents the irreversible lithium consumption by parasitic reactions, such as surface film formation and lithium plating. LAM indicates that the active material is no longer available for lithium intercalation and extraction that can occur at each electrode, and further clustered into LAM_{PE} for the PE and LAM_{NE} for the negative electrode. With the identified electrode parameters, the amount of different degradation can be quantified with the equations below.

The LLI can be represented by the reduction in the lithium inventory. At any point, total lithium inventory can be defined by the sum of lithium contents in the individual electrode. Since the stoichiometric states x and y are the degree of lithiation of the corresponding active material, the lithium content in one electrode can be calculated by multiplying the stoichiometric state to the capacity of the electrode (e.g., $Li_{PE} = y * C_p$). Therefore, the LLI is defined as follows:

$$LLI = 1 - \frac{y_{100}^a C_p^a + x_{100}^a C_n^a}{y_{100}^f C_p^f + x_{100}^f C_n^f} \tag{10}$$

where the superscript f represents the estimate from fresh cell and a for the aged cell. Similarly, the reduction in the estimated electrode capacities C_p and C_n directly indicates the LAM of positive and negative electrodes as follows:

$$LAM_{PE} = 1 - \frac{C_p^a}{C_p^f} \tag{11}$$

$$LAM_{NE} = 1 - \frac{C_n^a}{C_n^f} \tag{12}$$

where the superscript f represents the estimate from fresh cell and a for the aged cell.

B. Error Bound of Parameter Estimation

The goal of the identifiability analysis is twofold. One is to address if the unknown parameters are uniquely identified and, if it is uniquely determined, the second goal is to provide a measure of the reliability of the estimates out of the noisy output measurements. In this work, the CRB is used for quantifying the estimates' error bound for the electrode parameters. Note that the CRB is the lower bound of the variance for any unbiased estimator, and thus the error bound in this article is the best case scenario.

Suppose that a series of n observations $Y = [y_1, y_2, \ldots, y_n]$; in our case, the terminal voltage measurements of the cell are represented by the statistical model

$$y_j = f_j(\theta_0) + \epsilon_j, \quad j = 1, 2, \ldots, n \tag{13}$$

where f_j is the model in terms of the true parameter vector $\theta_0 \in \mathcal{R}^m$; in our case, f_j is the OCV model in (7) and $\theta_0 \in \mathcal{R}^4$ represents the capacity and utilization range of the individual electrodes. It is assumed the observation error ϵ_j are independent and identically distributed random variables with a zero mean

TABLE I
NOMINAL PARAMETERS FOR THE SELECTED NMC/GRAPHITE CELL

	Parameters	Values
Full- cell	C	4.95 Ah
	$V_{\max}$	4.2 V
	$V_{\min}$	3.0 V
Positive electrode	C_p	5.78 Ah
	$[y_{100}, y_0]$	[0.10, 0.95]
Negative electrode	C_n	6.24 Ah
	$[x_{100}, x_0]$	[0.81, 0.02]

and variance $var[\epsilon_j] = \sigma_0^2$. Then, with a series of measured output, the least square estimator $\hat{\theta}_{LS}$ becomes also a random variable following a sampling distribution, and the uncertainty of the estimation can be quantified from this distribution. Nonlinear regression approximation theory [17] describes that the estimator $\hat{\theta}_{LS}$ approximately follows a Gaussian distribution as sample size increases (i.e., asymptotically) under several regularity conditions and sampling conditions are met [18], [19]

$$\hat{\theta}_{LS} \sim \mathcal{N}_m(\theta_0, \sigma_0^2(\chi^T(\theta_0)\chi(\theta_0))^{-1} = \mathcal{N}_m(\theta_0, \Sigma_0) \tag{14}$$

where $\chi_{ij}(\theta)$ is $n \times m$ sensitivity matrix with elements that correspond to the sensitivity of the measured terminal voltage on each of the electrode parameters

$$\chi_{ij}(\theta) = \frac{\partial f_i(\theta)}{\partial \theta_j}. \tag{15}$$

Here, the true parameter θ_0 and the observation error variance σ_0 are unknown, the covariance matrix Σ_0 called unconstrained CRB must be approximated

$$\Sigma_0 = F^{-1} \approx \Sigma(\hat{\theta}) = \hat{\sigma}^2(\chi^T(\hat{\theta})\chi(\hat{\theta}))^{-1}, \tag{16}$$

where the matrix F is known as the Fisher information matrix and $\hat{\theta}$ is a parameter estimate obtained from the nonlinear least squares in (8a), and the approximation of the observation error variance $\hat{\sigma}^2$ of σ_0^2 is given by

$$\sigma_0^2 \approx \hat{\sigma}^2 = \frac{1}{n-m}\sum_{j=1}^{n}(f_j(\hat{\theta}) - y_j)^2. \tag{17}$$

Now, the sampling distribution of the estimator can be approximated with $\hat{\theta}$ as

$$\hat{\theta}_{LS} \sim \mathcal{N}_m(\theta_0, \Sigma_0) \approx \mathcal{N}_m(\hat{\theta}, \Sigma(\hat{\theta})). \tag{18}$$

Standard error (SE) to be used in the confidence interval calculation is defined as

$$SE(\hat{\theta}_k) = \left[\sqrt{\Sigma(\hat{\theta})}\right]_{kk}, \quad k = 1, 2, \ldots, m. \tag{19}$$

Finally, since both θ_0, Σ_0 are unknown and approximated as (18), the approximate confidence interval is constructed with t-distribution [18]

$$\hat{\theta}_k - t_{1-\alpha}SE(\hat{\theta}_k) \le \theta_k \le \hat{\theta}_k + t_{1-\alpha}SE(\hat{\theta}_k) \tag{20}$$

where $t_{1-\alpha}$ is the critical value of the t-distribution with the confidence level $(1-\alpha)\%$. The confidence level is the probability that the confidence interval contains the true parameter. Here, $t_{1-\alpha} = 2$ is used for 95% confidence level (i.e., $\alpha = 0.05$). Note that the interval in (20) is composed of the point estimate $\hat{\theta}_k$ and the margin of error that determines the uncertainty in the parameter estimation. Hence, the estimation error bound e_θ can be defined by the margin of error

$$e_{\theta_k}(\%) = t_{1-\alpha}\frac{SE(\hat{\theta}_k)}{\hat{\theta}_k} \times 100. \tag{21}$$

Observe that the SE term is divided by the least square estimate $\hat{\theta}_k$ for normalization, which enables the evaluation of the relative identifiability among all four electrode parameters.

If the estimation problem includes constraints to satisfy, the following procedure has to be additionally considered to determine the constrained CRB. The CRB under the parametric constraints can be found by a reparameterization of the original problem to remove redundancies in the parameter vector [20]. Consider a continuously differentiable constraint and its gradient matrix

$$h(\theta) = 0, \quad H(\theta) = \frac{\partial h(\theta)}{\partial \theta^T}. \tag{22}$$

If the gradient matrix $H(\theta)$ is full row rank, then one can find an orthogonal matrix U $(U^TU = I)$ whose columns form an orthonormal basis for the nullspace of $H(\theta)$. That is,

$$H(\theta)U = 0. \tag{23}$$

If $U^T\Sigma^{-1}U$ is nonsingular, then the parameters are identifiable and the constrained CRB (i.e., the error covariance matrix) can be obtained with some modifications

$$\Sigma'(\hat{\theta}) = U(U^T\Sigma^{-1}(\hat{\theta})U)^{-1}U^T. \tag{24}$$

Then, the SE term in (19) is recomputed with $\Sigma'(\hat{\theta})$ instead of $\Sigma(\hat{\theta})$. In our case, the voltage limit constraint (8b) ties up the utilization range of each electrode (y_{100} and x_{100}). And the gradient matrix $H(\theta)$ is full row rank where the first and third column entries are the nonzero local slope of the half-cell potential

$$\begin{aligned} H(\theta) &= \left[\frac{\partial U_p}{\partial y}\cdot\frac{\partial y}{\partial y_{100}} \quad 0 \quad -\frac{\partial U_n}{\partial x}\cdot\frac{\partial x}{\partial x_{100}} \quad 0\right] \\ &= \left[\alpha|_{y_{100}} \quad 0 \quad -\beta|_{x_{100}} \quad 0\right]. \end{aligned} \tag{25}$$

IV. RESULT AND DISCUSSION

In this section, the error bound of each electrode parameter is presented, and the dependence on different data window (DW) is investigated. For simulation, nominal parameters in Table I are used. The electrode parameters are estimated by fitting the OCV model to the full range of voltage data for a 5 Ah NMC/graphite cell. The details can be found in Section V-B.

A. Data Window

The concept of DW is defined to represent the partial availability of the OCV in the parameter estimation problem. Two points determine the location and size of the DW; starting-point Q_s; and end-point Q_e of the window, i.e., DW $= [Q_s, Q_e]$, as shown in Fig. 2 by the blue-shaded region. The differential voltage

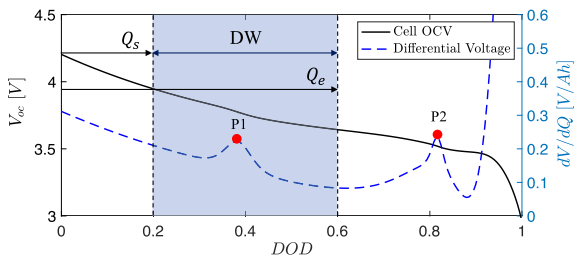

Fig. 2. Data window DW $= [Q_s, Q_e]$ of open-circuit voltage (OCV) is illustrated with respect to depth of discharge (DOD) to represent when only partial OCV curve data is available for parameter estimation.

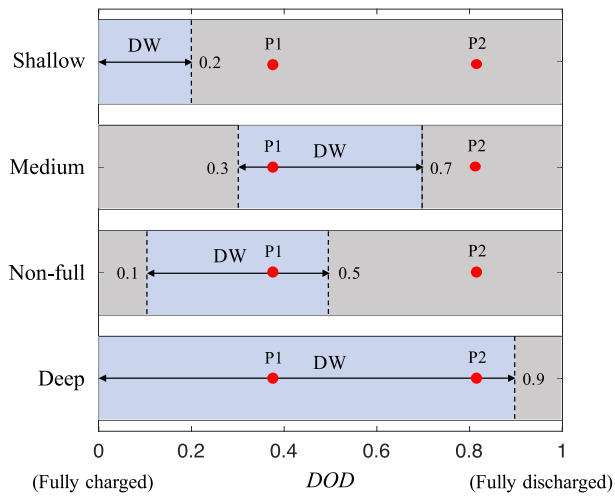

Fig. 3. Data windows (DWs) for different battery usage patterns. The peak locations (P1, P2) are also depicted.

(dV/dQ) curve is plotted on the right side of the y-axis with the indication of the two distinct peaks representing the phase transitions of the graphite NE. In [21], [22], it is shown that data taken from regions that include phase transitions of the electrode material improve the identifiability of the corresponding electrode parameters. Thus, the impact of the inclusion of peaks in DW will be discussed as well.

Various DWs are considered here with an assumption that the OCV data are partially available. For instance, if an electrified vehicle is used only for short commutes assuming full overnight charging is available, the battery would operate at high SOC range with small DOD. Similarly, range anxiety tends to make BEV drivers stay away from low SOC. Typical lower bound for the PHEV is designed to be around 30% SOC of the battery to protect against over-discharge and possible degradation. Thus, four different DWs are defined for a quantitative identifiability analysis on the electrode parameters: DW-shallow, medium, non-full, and deep as shown in Fig. 3. DW-shallow represents the condition that the battery is used down to 80% SOC. DW-medium and non-full demonstrate 40% of the battery capacity usages but utilized at different locations in the OCV curve, where the non-full represents not fully charged. Finally, DW-deep represents almost full range of the OCV curve is available.

B. Analytic Error Bounds of Electrode Parameters

Here, the error bounds, of which the SE term in (19) is defined by either (16) for the unconstrained case or (24) for the constrained case, are computed for all combination of the sizes and locations of DWs. Since the starting and end points are interchangeable and corresponding results are symmetric, the error bound results are drawn in a triangular-shaped plot with Q_s as y-axis and Q_e as x-axis in Fig. 4. Data points are evenly distributed with 0.5% DOD intervals. The observation error ϵ_j is assumed as a Gaussian white noise with a standard deviation of 10 mV. Note that the error bound is proportional to the observation error as shown in (16)–(21), and thus a larger measurement noise leads to larger error bounds making the estimation unreliable. A logarithmic scale color bar is adopted to highlight the transitions in the error bounds (e.g., the transition from the yellow to dark blue indicates a decrease of the error bound, and hence the more accurate estimation).

In terms of the DW, size and location are essential. First, a large size DW provides a small estimation error bound, and thus more accurate estimation can be achieved. Graphically speaking, as the DW becomes wider (i.e., $Q_s \to 0$ and $Q_e \to 1$), it approaches to the right bottom corner in the triangular plot in Fig. 4, which indicates the small error bound. Furthermore, for a quantitative analysis, the error bounds of the four predefined DWs are summarized in Fig. 5. The results in Fig. 5 are from the unconstrained and constrained CRBs verifying the impact of the voltage limit constraint on the estimation accuracy. The unconstrained case is discussed first in the following.

It is found that the half-cell potential slopes (α and β in Fig. 1) drive the identifiability of the electrode parameters. For NMC/graphite cell, the NMC PE potential has a relatively steeper slope than that of the graphite NE potential. This steeper slope provide better identifiability of the PE parameters (y_{100}, C_p) than that of the NE parameters (x_{100}, C_n). It can be found in Fig. 4 that the PE parameters show green color around the left bottom corner, meanwhile the NE parameters show yellow color indicating the PE parameters have better indentifiability or smaller error bounds than that of the NE. For the chemistry of LFP, it has a flat half-cell potential in the middle, and thus when only the flat voltage portion is utilized in a certain DW, the PE parameters are not observable. Meanwhile, when it is utilized over the range for the given DW that includes the very top charge level or deep discharge level, also known as knee or shoulder of the potential, the abrupt slope change provides ample information and makes the parameter estimation feasible [16], [21]. This observation explains the poorer estimation error for the DW-shallow than the others. When only the upper 20% range of battery capacity is used, all electrode parameters are not identifiable because of a lack of information. Large errors (above 30% break line) are obtained, except for the PE upper utilization range y_{100} as shown in Fig. 5. Even more so, the NE parameters are almost not identifiable due to large errors for the DW-shallow and non-full cases. This becomes understandable when the battery is depleted to the low SOC area, such as the DW-medium and deep cases where the NE half-cell potential

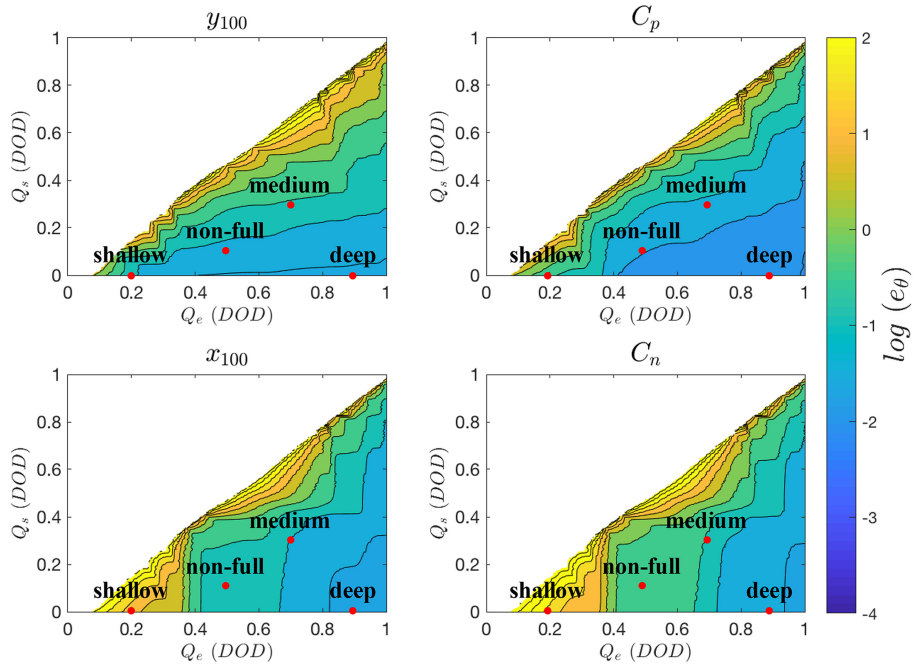

Fig. 4. Triangular plots for the analytic error bound of each electrode parameter in a logarithm scale. Four predefined data windows are indicated by red dots. Data points are evenly distributed with 0.5% depth of discharge (DOD) intervals and noise standard deviation σ =10 mV. No voltage constraint is considered.

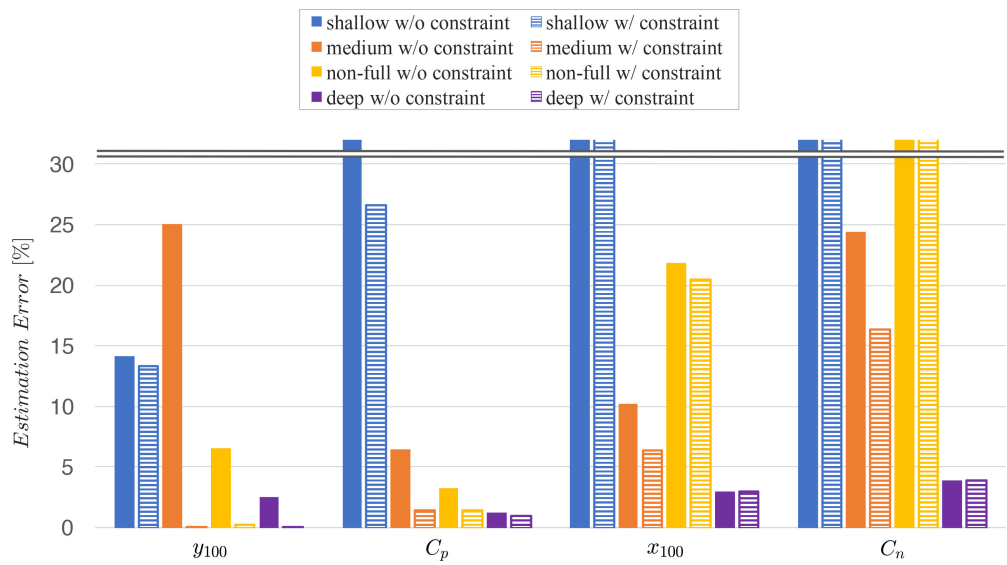

Fig. 5. Analytic error bound of each electrode parameter for various data windows. Results of both unconstrained (solid) and constrained (stripe pattern) cases are shown. Voltage limit constraint improves all the electrode parameters, especially for the positive electrode parameters.

increases and consequently the slope of the potential changes. Especially, for the DW-deep case, the utilized graphite anode potential rises significantly when the battery is almost fully depleted, making the estimation error of all electrode parameters less than 5%.

This improvement is also a benefit from the inclusion of the peaks inside the DW. As explained by Lee *et al.* [21], the slope change of the half-cell potential due to the phase transition improves the identifiability of the electrode parameters. Along with the phase transition, the potential undergoes a rapid change and results in the peak in the dV/dQ curve, as shown in Fig. 2, that provides ample information on the associated electrode parameters. Therefore, having a data range that includes these peaks provides better identifiability. For the graphite NE, distinct vertical transitions are observed in the NE parameters (x_{100}, C_n) as the end point Q_e increases in Fig. 4.

A comparison between two same-sized data windows, DW-medium vs. DW-non-full, the impact of the location of the DW can be explained. The non-full operates around a higher SOC region than that of the medium where the PE potential has a

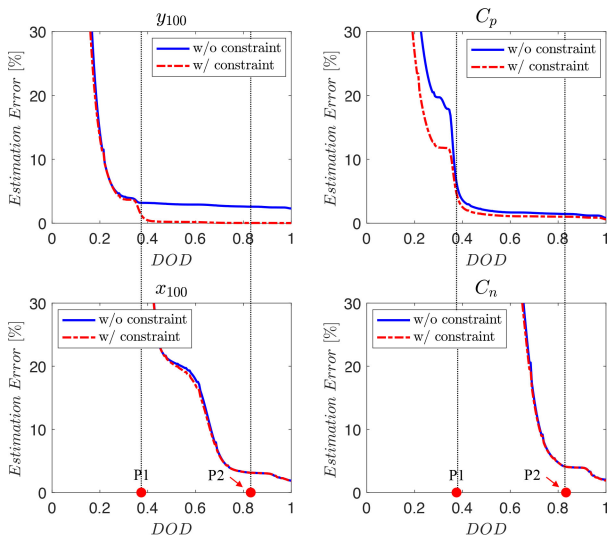

Fig. 6. Analytic error bound with respect to depth of discharge (DOD). As the size of data window increases, the error bound decreases with transitions around the peaks (P1, P2).

relatively steeper slope, and hence it provides better identifiability of the PE parameters for the non-full than that of the medium case. Similarly, when the relatively low SOC region is utilized as in the medium case, the relatively steeper slope of the graphite NE provides better identifiability of the NE parameters in the medium.

C. Impact of Voltage Constraint

The optimization problem in (8) has a nonlinear equality constraint for the upper voltage limit. In this case, the constrained CRB is used for computing the error bound. The voltage constraint ties the upper utilization ranges of each electrode (y_{100} and x_{100}), which provides the parameter dependency between the positive and negative electrodes, which in turn reduces the number of unknown parameters and consequently improves the estimation accuracy (see Fig. 5; the error bounds of the PE parameters become significantly improved, especially the utilization range y_{100} becomes less than 0.3% for all the DWs except the DW-shallow case). Parameter dependency can be explained by using the Taylor series expansion of the voltage constraint about the nominal parameters

$$\sigma_y \left.\frac{\partial U_p}{\partial y}\right|_{y_{100}} = \sigma_x \left.\frac{\partial U_n}{\partial x}\right|_{x_{100}}. \tag{26}$$

Comparing local slope of the half-cell potentials ($\alpha = \frac{\partial U_p}{\partial y}|_{y_{100}}$ and $\beta = \frac{\partial U_n}{\partial x}|_{x_{100}}$ in Fig. 1), β is smaller than α due to the flat voltage curve of the graphite NE. Hence, the error bound σ_x is larger than σ_y. Furthermore, since the parameters from the same electrode are correlated, the improvement in the estimation accuracy of y_{100} is beneficial to the estimation accuracy of C_p as well. More clear effects of the size of the DW and the peak information can be found in Fig. 6. Here, the estimation error bounds of each electrode parameters are plotted with respect to DOD. All of the error bound decreases as more data points are included in the DW, which indicates the impact of the provided information on the estimation accuracy. Moreover, the error bound decreases with the transition around the peaks. Especially, the estimation error bounds of the PE parameters show a sharp transition at P1 location, DOD = 0.4. Similarly, the transitions occur at both peak points for the NE parameters. Since the slope of the graphite NE potential starts to change before P2 location, the transitions of the error bound in the NE parameters occur around DOD = 0.7.

TABLE II
ESTIMATION ERROR BOUND FOR UNCONSTRAINED CASE

without constraint	Error bound e_{θ_k} (%)			
	$\theta_1 = y_{100}$	$\theta_2 = C_p$	$\theta_3 = x_{100}$	$\theta_4 = C_n$
MC simulation	2.5	1.3	3.0	3.9
Analytic derivation	2.5	1.3	3.0	3.9

TABLE III
ESTIMATION ERROR BOUND FOR CONSTRAINED CASE

with constraint	Error bound e_{θ_k} (%)			
	$\theta_1 = y_{100}$	$\theta_2 = C_p$	$\theta_3 = x_{100}$	$\theta_4 = C_n$
MC simulation	3.2e-2	0.9	3.0	3.9
Analytic derivation	3.0e-2	0.9	3.0	3.9

V. VALIDATION

A. Numerical Validation

Given the error bound based on the CRB, this section presents numerical simulation results obtained from a Monte–Carlo (MC) simulation to verify the analytic derivation. The parameter estimation has been repetitively conducted for 1000 times for both the unconstrained case and the constrained case based on both (8a) and (8b). The voltage data is simulated by the OCV model in (7) with the nominal electrode parameters in Table I and the additive zero-mean Gaussian voltage error with a standard deviation of $\sigma = 10$ mV. The DW-deep case is selected that utilizes 90% of the battery capacity from the fully charged state.

From the MC simulation, the estimation errors of each electrode parameters are calculated based on the nominal parameters in Table I. Then, these errors are drawn on scatter plots along with a histogram in Fig. 7, verifying the distribution of the estimated electrode parameters is approximately a Gaussian, which agrees with the aforementioned approximation theory. Observe that the estimation errors are centered at near zero indicating the estimates are unbiased. Since the estimator is unbiased, the error bound obtained from the CRB can be considered as a proper metric for our electrode parameter estimation problem. The error bounds of all four electrode parameters at the 95% confidence level show a good agreement with the numerical MC simulation results for both the unconstrained and constrained cases (see Tables II and III). Hence, this agreement verifies the derivation of the analytic error bound. In addition to that, for

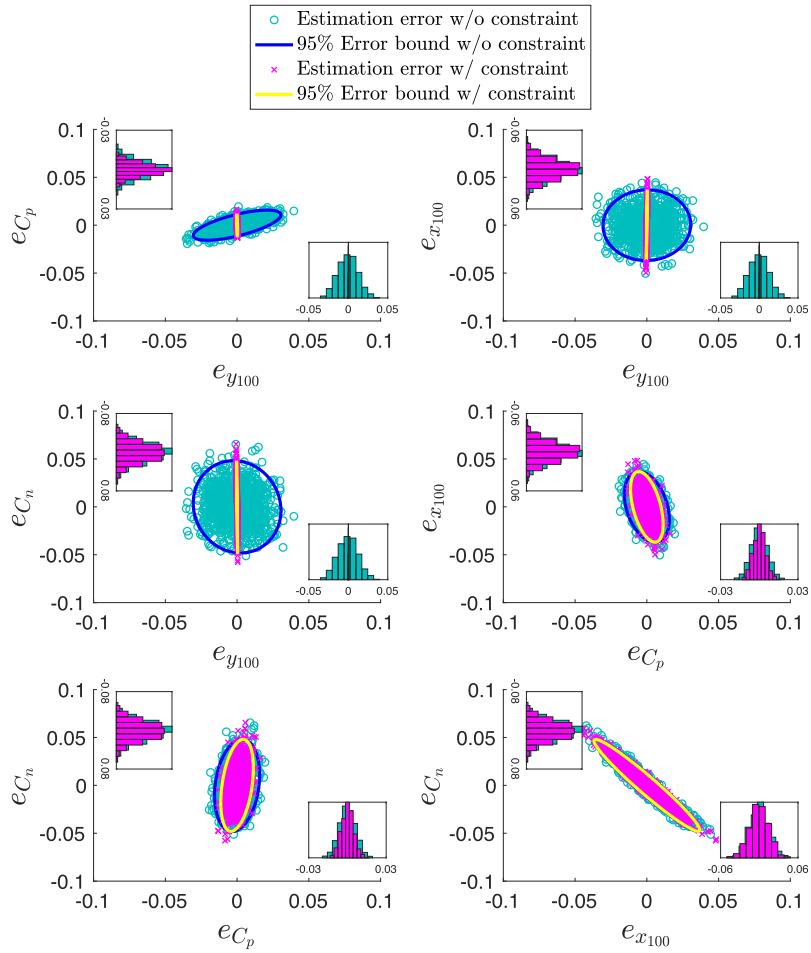

Fig. 7. Scatter plot of the electrode parameter estimation errors from Monte–Carlo simulation for the DW-deep case (i.e., DW = [0, 0.9]). Estimation errors show approximate normal distribution. The 95% confidence-level error bound (solid line) agrees with the simulation results.

the unconstrained case, a strong correlation has been observed among the parameters from the same electrode, either from the PE or NE, as shown in the top left ($e_{y_{100}}$ vs. e_{C_p}) and bottom right ($e_{x_{100}}$ vs. e_{C_n}) plots in Fig. 7. However, the parameters from the different electrodes do not show any correlation. Comparing Tables II and III, the parameter dependency in (26) improves the estimation accuracy, especially for the PE parameters.

B. Experimental Validation

In this section, the parameter estimation is done for a 5 Ah NMC/graphite cell at different data availabilities to experimentally validate the proposed analytic error bounds. Pseudo-OCV data are measured at C/20 rate of constant current from fully charged state, and the half-cell potentials of each electrode are also individually measured from a coin cell referenced by the lithium metal counter electrode. Then, the electrode parameter values are estimated by fitting the OCV model to the voltage data using a nonlinear least-squares estimation as illustrated in (8), including the voltage equality constraint.

To validate the proposed results, the estimates from full-range data are set as a baseline and compared with the estimated parameter values from the predefined DWs to quantify estimation errors. In Fig. 8(a), the measured data and the model estimate show a good fit. The voltage errors are spread symmetrically centered at zero such that the assumption on the zero-mean

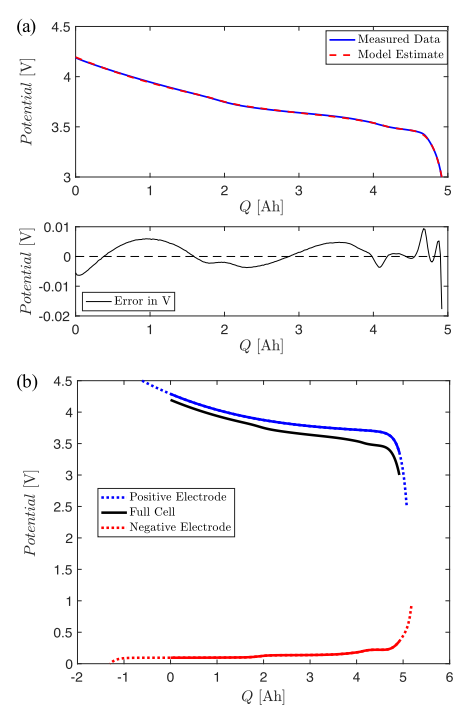

Fig. 8. Parameter estimation results for the given full-range data of a NMC/graphite cell. (a) Measured data and model fit with an error plot. (b) Decoupled voltage curves for each electrode; utilized range is marked with solid line and full electrode range is represented by dashed line.

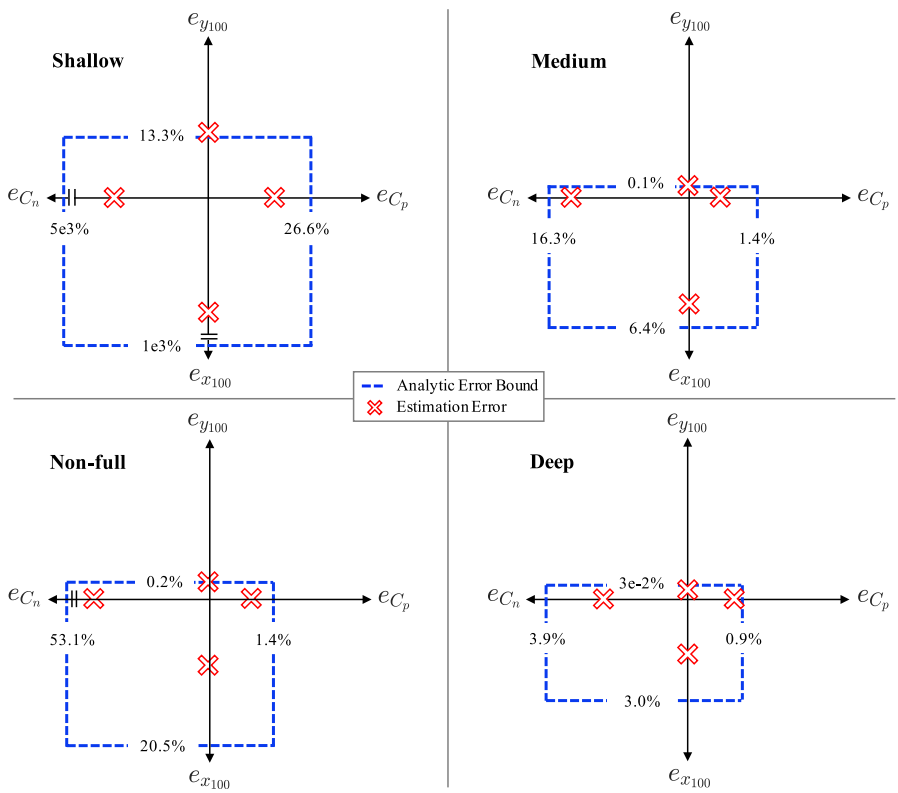

Fig. 9. Estimation errors for the electrode parameters under different data windows. Most of the estimation errors are inside the analytic error bounds validating the proposed results (graph is not to scale).

TABLE IV
ESTIMATION ERRORS FOR THE ELECTRODE PARAMETERS UNDER DIFFERENT DATA WINDOWS

Data Window ID	Data window range	Experimental estimation error e_θ (%)			
		$\theta_1 = y_{100}$	$\theta_2 = C_p$	$\theta_3 = x_{100}$	$\theta_4 = C_n$
Shallow	[0.0, 0.2]	14.9	16.8	38.3	24.1
Medium	[0.3, 0.7]	0.1	0.4	4.9	14.5
Non-full	[0.1, 0.5]	0.2	0.9	10.0	24.1
Deep	[0.0, 0.9]	0.0	0.8	1.6	1.8

observation error holds. Fig. 8(b) shows decoupled voltage curves for both electrodes with an indication for the utilized range (solid lines) along with the full electrode capacity range (dashed lines). Here, the graphite NE has more total electrode capacity; thus, the electrode capacity range (red dashed line) is larger than that of the NMC PE (blue dashed line). Detailed information on the parameter estimation can be found in [5], [6], [21].

Fig. 9 and Table IV summarize the relative estimation errors obtained from the predefined DWs. Fig. 9 shows that most of the errors are inside the error bounds except $e_{y_{100}}$ for the DW-shallow case. Note that the error bounds do not necessarily predict exact error values for a given DW, but describe a boundary for error statistics. From Fig. 9 and Table IV, not only the inclusion of the estimation errors is validated, but also the effects of different DWs can be found. The DW-deep shows the smallest estimation errors where almost all data range is available. Like in the analytic error bound results in Fig. 5, comparing two DWs, the medium and the non-full, that have the same span but at different location, the medium case shows relatively smaller estimation errors especially for the negative electrode parameters (x_{100} and C_n) because the utilization range of the electrode becomes more informative as the DW gets closer to a deeper discharged area.

VI. GUIDELINE FOR SELECTING DATA WINDOW

In this section, we propose a guideline that explains how this framework can be used for selecting a proper DW to achieve the desired estimation accuracy. Suppose we have a series of

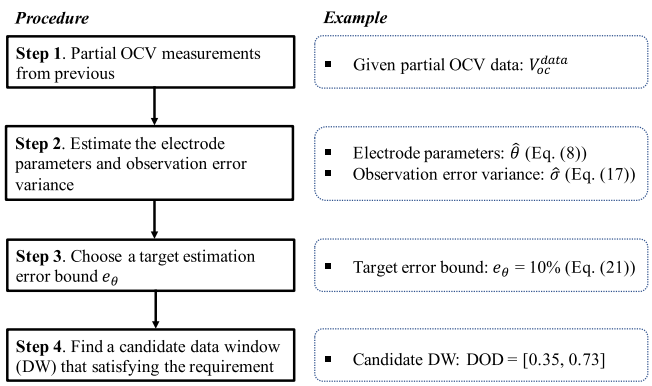

Fig. 10. Flowchart for selecting a proper data window associated with the required estimation error bound for the electrode state of health parameters.

OCV measurements from a partial DOD, of which observation error is characterized by zero mean and $\hat{\sigma}^2$ variance. If a target estimation error bound is given, we can find the required DW as illustrated in the flowchart of Fig. 10. For instance, if the given voltage error variance $\hat{\sigma} = 10$ mV and the target error bound is within 10% at a 95% confidence level, the OCV range of DOD = [0.35, 0.73] can be one possible DW satisfying the requirement.

VII. Conclusion

In this article, the estimation uncertainty of the electrode parameters was quantified with a focus on the limited availability of OCV data. Conventionally, these parameters were identified with a full range of OCV data, which is not practical for many applications. In realistic scenarios, OCV data are difficult to measure due to the time limit; hence, OCV data are likely limited to an incomplete DW. When such OCV data are limited, the estimation suffers from the loss of accuracy; hence, the reliability of the estimation results has to be questioned.

Analytical error bound of the electrode parameters were derived based on the CRB and confidence interval. The derived error bounds agreed with the numerical MC simulation as well as the experimental results obtained from 5 Ah NMC/graphite cell. It is found that the DW plays a vital role in the estimation accuracy associated with the local slope of the half-cell potential. In general, the PE parameters have a better identifiability than the negative electrode (NE) parameters because of a relatively higher local slope in an NMC/graphite chemistry cell. Furthermore, the PE parameters can be even more accurately estimated by introducing a voltage constraint in the estimation problem. On the other hand, when only a small portion of data is available, the estimation accuracy of the graphite NE parameters is reduced, resulting in a large error bound. Therefore, one must consider estimation uncertainty when the DW is limited.

The results and framework presented here can be extended in several directions in future work. First, the analysis here was based on a set of simplifying assumptions, including that the half-cell potentials of both electrodes are available and these potentials are invariant. Model mismatch due to cell-to-cell variance or aging can be a source of additional estimation error; hence, the propagation of the model mismatch to the parameter estimation will be clarified in future work. Second, a way to acquire the desired DW needs to be addressed in real-world applications. For example, we can optimize a charging protocol that allows acquiring a portion of pseudo-OCV measurement and charges the battery as requested within a given charging time.

References

[1] S. J. Moura, J. C. Forman, S. Bashash, J. L. Stein, and H. K. Fathy, "Optimal control of film growth in lithium-ion battery packs via relay switches," *IEEE Trans. Ind. Electron.*, vol. 58, no. 8, pp. 3555–3566, Aug. 2011.

[2] G. K. Prasad and C. D. Rahn, "Model based identification of aging parameters in lithium ion batteries," *J. Power Sources*, vol. 232, pp. 79–85, 2013.

[3] M. Dubarry, C. Truchot, and B. Y. Liaw, "Synthesize battery degradation modes via a diagnostic and prognostic model," *J. Power Sources*, vol. 219, pp. 204–216, 2012.

[4] C. R. Birkl, M. R. Roberts, E. McTurk, P. G. Bruce, and D. A. Howey, "Degradation diagnostics for lithium ion cells," *J. Power Sources*, vol. 341, pp. 373–386, 2017.

[5] X. Han, M. Ouyang, L. Lu, J. Li, Y. Zheng, and Z. Li, "A comparative study of commercial lithium ion battery cycle life in electrical vehicle: Aging mechanism identification," *J. Power Sources*, vol. 251, pp. 38–54, 2014.

[6] S. Lee, J. B. Siegel, A. G. Stefanopoulou, J.-W. Lee, and T.-K. Lee, "Comparison of individual-electrode state of health estimation methods for lithium ion battery," in *Proc. ASME Dyn. Syst. Control Conf.*, 2018, vol. 2, Paper V002T19A002.

[7] S. Dey, Y. Shi, K. Smith, A. Colclasure, and X. Li, "From battery cell to electrodes: Real-time estimation of charge and health of individual battery electrodes," *IEEE Trans. Ind. Electron.*, vol. 67, no. 3, pp. 2167–2175, Mar. 2019.

[8] S. Lee, Y. Kim, J. B. Siegel, and A. G. Stefanopoulou, "Minimum-time measurement of open circuit voltage of battery systems," in *Proc. IEEE Amer. Control Conf.*, 2019, pp. 884–889.

[9] ClipperCreek. (2018). Charging time chart. [Online]. Available: https://www.clippercreek.com/charging-times-chart

[10] A. Sharma and H. K. Fathy, "Fisher identifiability analysis for a periodically-excited equivalent-circuit lithium-ion battery model," in *Proc. IEEE Amer. Control Conf.*, 2014, pp. 274–280.

[11] X. Lin and A. G. Stefanopoulou, "Analytic bound on accuracy of battery state and parameter estimation," *J. Electrochem. Soc.*, vol. 162, no. 9, pp. A1879–A1891, 2015.

[12] X. Lin, "Analytic analysis of the data-dependent estimation accuracy of battery equivalent circuit dynamics," *IEEE Control Syst. Lett.*, vol. 1, no. 2, pp. 304–309, Oct. 2017.

[13] X. Lin, Y. Kim, S. Mohan, J. B. Siegel, and A. G. Stefanopoulou, "Modeling and estimation for advanced battery management," *Annu. Rev. Control, Robot., Auton. Syst.*, vol. 2, pp. 393–426, 2019.

[14] C. Edouard, M. Petit, C. Forgez, J. Bernard, and R. Revel, "Parameter sensitivity analysis of a simplified electrochemical and thermal model for Li-ion batteries aging," *J. Power Sources*, vol. 325, pp. 482–494, 2016.

[15] J. C. Forman, S. J. Moura, J. L. Stein, and H. K. Fathy, "Genetic identification and Fisher identifiability analysis of the Doyle–Fuller–Newman model from experimental cycling of a LiFePO4 cell," *J. Power Sources*, vol. 210, pp. 263–275, 2012.

[16] P. Mohtat, S. Lee, J. B. Siegel, and A. G. Stefanopoulou, "Towards better estimability of electrode-specific state of health: Decoding the cell expansion," *J. Power Sources*, vol. 427, pp. 101–111, 2019.

[17] G. Sever and C. Wild, *Nonlinear Regression*. Hoboken, NJ, USA: Wiley, 2003.

[18] H. Banks, S. L. Ernstberger, and S. L. Grove, "Standard errors and confidence intervals in inverse problems: Sensitivity and associated pitfalls," *J. Inverse Ill-Posed Problems*, vol. 15, no. 1, pp. 1–18, 2007.

[19] Z. Chen, L. Y. Wang, G. Yin, F. Lin, and C. Wang, "Accurate probabilistic characterization of battery estimates by using large deviation principles for real-time battery diagnosis," *IEEE Trans. Energy Convers.*, vol. 28, no. 4, pp. 860–870, 2013.

[20] P. Stoica and B. C. Ng, "On the Cramér–Rao bound under parametric constraints," *IEEE Signal Process. Lett.*, vol. 5, no. 7, pp. 177–179, Jul. 1998.

[21] S. Lee, P. Mohtat, J. B. Siegel, and A. G. Stefanopoulou, "Beyond estimating battery state of health: Identifiability of individual electrode capacity and utilization," in *Proc. IEEE Am. Control Conf.*, 2018, pp. 2288–2293.

[22] H. M. Dahn, A. Smith, J. Burns, D. Stevens, and J. Dahn, "User-friendly differential voltage analysis freeware for the analysis of degradation mechanisms in Li-ion batteries," *J. Electrochem. Soc.*, vol. 159, no. 9, pp. A1405–A1409, 2012.

Suhak Lee received the B.S. degree in mechanical engineering from the Seoul National University, South Korea, in 2011. He is currently working toward the Ph.D. degree in mechanical engineering with the University of Michigan, Ann Arbor, MI, USA.

He was with STX Engine, South Korea, from 2011 to 2013, and Korean Air, South Korea, from 2013 to 2014. His current research interests include state of health estimation, diagnostics, and remaining useful life prediction based on model-based and data-driven machine learning approaches. He was involved in projects on optimal control, degradation diagnostics, and prognostics of energy storage systems and various mechanical components.

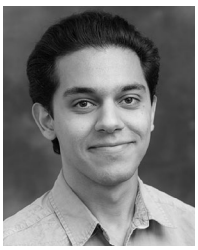

Peyman Mohtat received the B.S. degree in mechanical engineering from the University of Tehran, Iran, in 2015, and the master's degree in mechanical engineering in 2017 from the University of Michigan, Ann Arbor, MI, USA, where he is currently working toward the Ph.D. degree in mechanical engineering.

His research interests include physics-based modeling for lithium-ion batteries and fuel cells. He was involved in projects on battery degradation diagnostics using cell swelling and data-driven models for fuel cells.

Jason B. Siegel received the bachelor's and the Ph.D. degrees in electrical engineering from the University of Michigan, Ann Arbor, MI, USA, in 2004 and 2010, respectively.

After a two-year postdoc, he joined the faculty as a Research Scientist with the Department of Mechanical Engineering, University of Michigan, in 2012. His research interests include physics-based modeling and control of energy storage and conversion systems including lithium-ion batteries and proton exchange membrane fuel cells. He has coauthored more than 30 journal articles.

Dr. Siegel is the Chair of the IEEE Technical Committee on Automotive Control.

Anna G. Stefanopoulou (F'09) is the William Clay Ford Professor and the Director of the Energy Institute, University of Michigan, Ann Arbor, MI, USA. She was an Assistant Professor with the University of California, Santa Barbara, CA, USA, and a Technical Specialist with the Ford Motor Company. She has coauthored a book, and have 21 U.S. patents, and more than 340 publications (seven of which have received awards) on estimation and control of internal combustion engines and electrochemical processes such as fuel cells and batteries.

Dr. Stefanopoulou is a Fellow of the American Society of Mechanical Engineers (ASME) (2008) and Society of Automobile Engineers (SAE) (2018), and Elected Member of the Executive Committee of the ASME Dynamics Systems and Control Division, and the Board of Governors of the IEEE Control System Society. She has received multiple awards in powertrain control technology and has been a member of U.S. National Academies committees on light duty vehicle fuel efficiency.

Jang-Woo Lee received the M.S. degree in physics from the MIT, Cambridge, MA, USA, and the B.S. and M.S. degrees in physics from the Korea University, South Korea.

He is currently an Engineer with the Samsung SDI, South Korea, working in battery system research and development, including battery modeling and simulation for the BMS SW and algorithms. While at SDI, he worked for over ten years in both the R&D Center and System Development Team with special interest in the battery degradation mechanism. Before joining SDI, he did research in experimental particle and nuclear physics at the K2K neutrino experiment at KEK, Japan, the ZEUS electron–proton experiment at DESY, Germany, the PHOBOS experiment at RHIC, USA, and the CDF experiment at Fermilab, USA.

Tae-Kyung Lee received the B.S. and M.S. degrees from Seoul National University, South Korea, in 1996 and 1998, respectively, and the Ph.D. degree from the University of Michigan, Ann Arbor, MI, USA, in 2009, all in mechanical engineering.

He is currently the Vice President of Samsung SDI, South Korea, in charge of battery system research and development, including mechanical designs, simulations, and battery management system (BMS) HW/SW/algorithms. Before joining Samsung SDI, he worked with Ford Motor Company, Dearborn, MI, USA, served as a Research Scientist with the Department of Mechanical Engineering, University of Michigan, Ann Arbor, USA, and worked with Hyundai Motor Company (HMC), South Korea. He is the author of over 36 international journal and conference articles, and 34 U.S. patents.

Dr. Lee is the recipient of the IMechE Donald Julius Groen Award (2011) by the Institution of Mechanical Engineers (IMechE) Mechatronics, Informatics and Control Group, and Springer Award (2012) by the *International Journal of Automotive Technology*.